Front. Struct. Civ. Eng. 2025, 19(8): 1222–1239
https://doi.org/10.1007/s11709-025-1209-0

RESEARCH ARTICLE

Structural evaluation of the novel connection system between adjacent breakwater caissons

Seungbok LEE[a,b], Kyeongjin KIM[c], Meeju LEE[a,b], Jeongho KIM[a,b], Seokmun KIM[d], Jaeha LEE[a,b*]

[a] *Department of Civil Engineering, National Korea Maritime & Ocean University, Busan 49112, South Korea*
[b] *Interdisciplinary Major of Ocean Renewable Energy Engineering, National Korea Maritime & Ocean University, Busan 49112, South Korea*
[c] *K-BETS (Korea Blue Energy Total Solution Co., Ltd.), Seoul 06530, South Korea*
[d] *Buman Engineering Co., Ltd., Gyeongsangnam-do 52563, South Korea*
[*] *Corresponding author. E-mail: jaeha@kmou.ac.kr*

ABSTRACT Climate change is having an increasing impact on coastal infrastructure, leading to more frequent and intensified wave activity, including higher waves driven by typhoons and abnormal sea conditions. Consequently, issues related to the stability of existing port structures, such as caissons, have become a significant concern. In particular, gravity-type caisson on the land side of coastal port structures require enhanced stability and safety. Gravity-type caissons, which resist external forces through their own weight, are highly vulnerable to functional failures, such as sliding displacement, triggered by abnormal waves shifting specific caissons. The destruction of caisson and quay walls can lead to substantial recovery costs, necessitating improvements in caisson stability to address the challenges posed by increased wave forces and changes in port logistics due to larger vessels. One approach to enhancing caisson stability is the use of long caissons. Long caisson is commonly used where a breakwater is needed to withstand wave action and distribute forces evenly along a length of breakwater. The construction of caissons faces challenges due to limitations on the size of individual units imposed by construction conditions, launching methods, and marine crane requirements. Therefore, connecting multiple caissons to form long caissons presents a viable alternative. This study suggested two connection methods for long caissons. The first method was a hemisphere caisson, which allows the connection parts to seat against each other under self-weight during construction. The second method was a displacement-allowing connection utilizing rubble (embedded rebar connection within riprap connection). This approach allows some displacement while employing rebar to resist excessive deformation, thereby dispersing the resulting wave forces to adjacent caissons. Performance comparisons between the developed connections and conventional gravity-type caissons were conducted using a finite element analysis model. The results indicate that the proposed connections demonstrate improved resistance to wave forces compared to traditional caissons without such connections. Further studies should include field applications and performance evaluations of various caisson sizes under different environmental and geological conditions.

KEYWORDS interlocking caisson, hemisphere connection, deformable joint, marine concrete structures, discrete element method-finite element method coupling analysis

1 Introduction

Most breakwater systems rely primarily on their self-weight to maintain structural stability. However, rising sea levels and the intensification of wave forces have increased the vulnerability of certain caisson-type breakwaters to sliding and overturning under extreme conditions [1]. A representative example is the 2011 Tohoku Pacific Coast Earthquake, during which liquefaction of the foundation soil, induced by seismic

Article history: Received Mar 5, 2025; Accepted May 14, 2025

vibrations, led to caisson subsidence. This significantly impaired the caisson’s ability to reflect waves and dissipate energy. Consequently, significant research efforts have been dedicated to reinforcing the foundation soils beneath caissons and addressing the combined effects of earthquakes and tsunamis [2–8]. In addition to ground improvement methods, an alternative approach to improving the stability of caisson breakwaters involves modifying their structural dimensions. To bolster the inherent stability of these structures, the use of larger caisson designs has been increasingly implemented [9]. Takahashi and Shimosako [10] demonstrated that increasing the size of caissons substantially improves their resistance to sliding and overturning. However, large caissons entail high construction and transportation costs due to their onshore prefabrication, the need for heavy lifting equipment, and large installation spaces. To mitigate these limitations, recent studies have focused on improving stability through interconnection systems between caissons [11–14]. In this study, two types of novel caisson connection systems were developed and evaluated, both utilizing interlocking mechanisms to improve stability. The first system, illustrated in Fig. 1(a), features a hemispherical protrusion on the upper joint surface, aligned with a corresponding recess on the lower joint. This configuration enables a self-aligning effect during installation, simplifying construction. Moreover, the hemispherical interface allows minor sliding and controlled displacement under wave-induced loads, which helps to absorb shocks and reduce stress concentration at the joint. Despite these advantages, the shear resistance performance of this connection has not yet been quantitatively evaluated. Therefore, this study investigates the influence of design parameters, such as hemisphere diameter and embedment depth, on shear performance. The second system, shown in Fig. 1(b), is

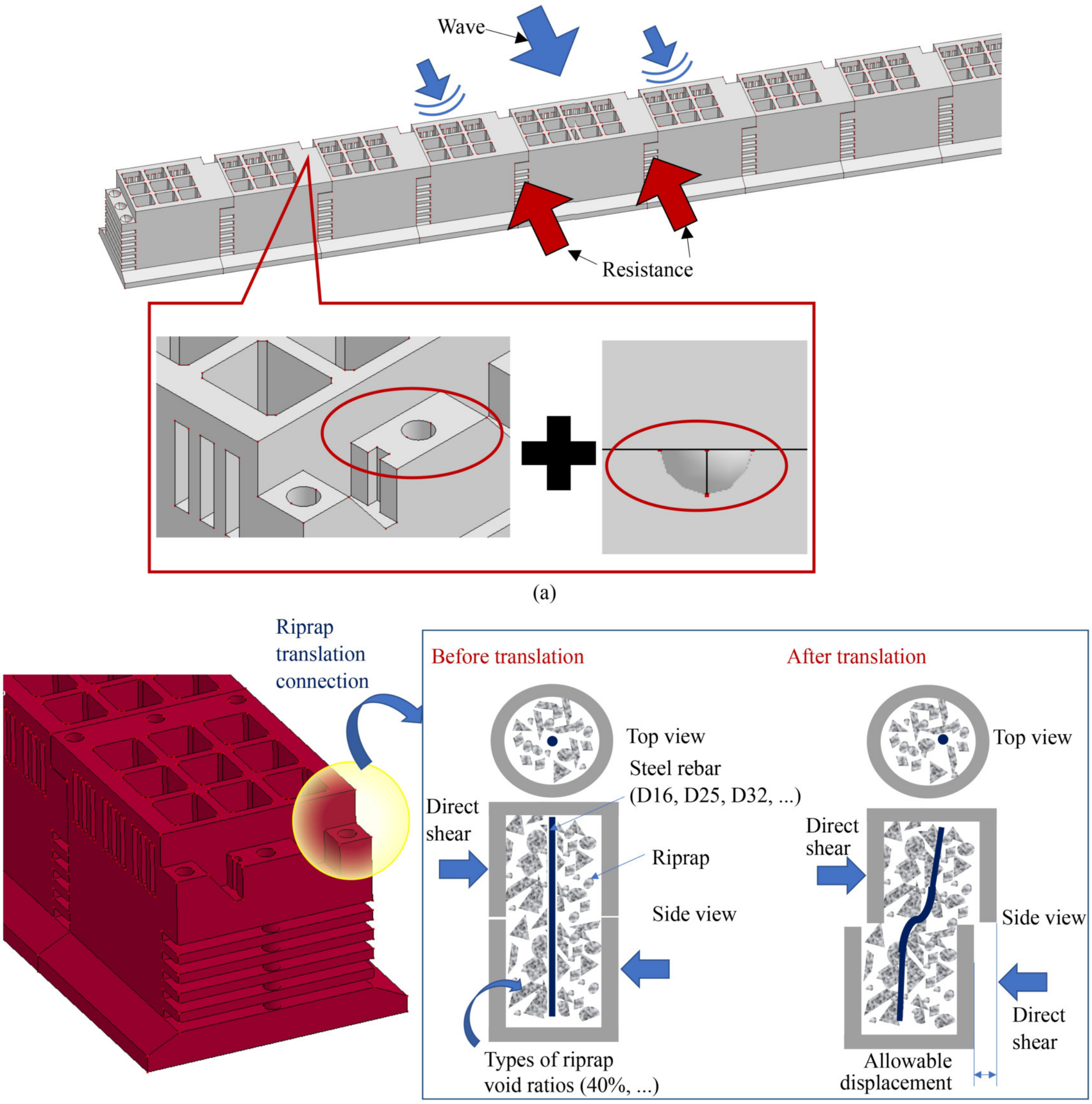

(a)

(b)

Fig. 1 Developed novel connection systems: (a) hemisphere connection; (b) ERCR.

the embedded rebar connection within riprap (ERCR). This method introduces void spaces at the upper and lower joint regions, which are filled with riprap and reinforcing bars. Under wave loading, the riprap mobilizes in the direction of resistance, allowing partial displacement while increasing interlocking resistance. The interaction between the riprap and the embedded rebar permits minor movement under low loads but resists larger displacements by transferring forces to adjacent caissons, thereby achieving load distribution and reducing stress concentration at the joints. To evaluate the mechanical performance of these systems, finite element (FE) models were developed. Structural resistance under wave-induced forces was assessed for both connection types. Furthermore, the proposed connection systems were applied to full-scale long caisson structures to evaluate their global stability and effectiveness in dissipating wave forces.

2 Numerical model for developed novel connections

In this study, numerical analyses were performed on two types of connection systems designed to improve the structural performance of caisson breakwaters. The first system, referred to as the hemisphere connection, incorporates a hemispherical joint geometry that enhances constructability by facilitating self-alignment under self-weight, thereby improving installation accuracy even in the presence of minor initial misalignments. The second system, known as the ERCR, is a cost-effective solution that utilizes riprap and reinforcing steel bars to resist wave-induced forces. When a caisson experiences displacement due to wave action, stress is concentrated at the connection—a structurally vulnerable location. The ERCR connection is designed to accommodate a controlled level of displacement, allowing it to effectively dissipate and redistribute stress concentrations. Previous studies by Kim et al. [15,16] have demonstrated that such an approach contributes to reducing damage caused by external loads. The performance of the hemisphere connection was evaluated using a FE model, while the ERCR connection was analyzed through a coupled discrete element method-finite element method (DEM-FEM) coupling analysis model to account for the interaction between riprap and rebar. Finally, the overall structural performance of the proposed connection systems was assessed in full-scale caisson models using FE analysis, focusing on their stability against sliding and overturning under wave-induced loading.

2.1 The continuous surface cap (CSC) material model for hemisphere connections

The finite element method (FEM) was selected as the analysis approach for the structural model. For the concrete material, the CSC model was adopted [17]. The CSC model has been widely used to simulate the behavior of concrete, as demonstrated in previous studies [15,16,18–21]. Originally developed by the Federal Highway Administration (FHWA) in the United States for roadside safety applications, the CSC model is capable of capturing multi-axial strength, strain rate effects, element erosion, fracture energy, and strength degradation. Detailed information on the CSC model is available in Ref. [22]. One of the key parameters in the CSC model is the erode value, which governs the removal of highly damaged elements after impact. This threshold has a direct influence on simulation outcomes and must therefore be selected with care. While an erode threshold of 1.1 has been commonly suggested, a value of 1.4 was adopted in the present study based on the findings of Refs. [16,23]. A comparative study was also conducted to justify the selected erode value. Another critical parameter is the fracture energy, which can be estimated using the method proposed in Ref. [24], as expressed in Eqs. (1) and (2):

$$f_{\mathrm{ctm}} = 0.3(f_{\mathrm{ck}})^{2/3}, \tag{1}$$

$$G_{\mathrm{F}} = 73 \times f_{\mathrm{cm}}^{0.18}, \tag{2}$$

where f_{ctm} is the tensile strength, f_{ck} is the characteristic compressive strength, G_{F} is the fracture energy of concrete, f_{cm} is the mean compressive strength at the age of 28 d. For the numerical model, the key parameters selected for the continuous surface cap model (CSCM) were as follows: an erode value of 1.4, a compression softening parameter of 10, a tension softening parameter of 0.1, and a repow value of 1.0. The coefficient repow enhances the strength due to the strain effect in CSCM. In the CSCM, the fracture energy of concrete can be calculated automatically. However, the fracture energy computed by the CSCM's default method is based on the predictive formula provided by Comite Euro-International Du Beton (CEB)-fib 1990 [25], which differs from more recent fracture energy predictions. Consequently, the fracture energy was manually calculated using a contemporary predictive formula and applied to the model (CEB-fib 2010) [24]. A detailed analysis of the variable selection for key parameters is presented in Kim et al. [26].

2.2 The discrete element method for embedded rebar connection within riprap connections

In this study, riprap was modeled using the DEM. Unlike the FEM, which treats the entire system as a continuum and obtains solutions, DEM considers the system as a collection of individual particles and obtains solutions. In most cases, discrete elements are assumed to be rigid, and their displacement and contact forces are calculated based on their movements. The forces acting on discrete elements are determined by the displacement and contact force between two contacting elements. According to Cundall and Strack, the motion of the elements is recalculated at each time step, and the contact force and vectors (normal vector, tangential vector) between two discrete elements are expressed by the following equations [27]:

$$F_i = F_i^{\mathrm{n}} + F_i^{\mathrm{s}}, \tag{3}$$

where F_i^{n} is normal vector, F_i^{s} is shear vector, and F_i is contact force. The normal contact force vector and total shear force is expressed as:

$$F_i^{\mathrm{n}} = K^{\mathrm{n}} U^{\mathrm{n}} n_{\mathrm{o}}, \tag{4}$$

$$F_i^{\mathrm{s}} = \{F_i^{\mathrm{s}}\}^{\mathrm{Current}} \Delta F_i^{\mathrm{s}}, \tag{5}$$

$$\Delta F_i^{\mathrm{s}} = -K^{\mathrm{s}} V_i^{\mathrm{s}} \Delta t, \tag{6}$$

where U^{n} is overlapping displacement of the two entities in contact, n_{o} is the unit normal vector, and K^{n} is normal stiffness at contact. $\{F_i^{\mathrm{s}}\}^{\mathrm{Current}}$ is the updated shear force in every time step and ΔF_i^{s} is the incremental shear force. K^{s} is the shear contact stiffness, V_i^{s} is the shear component of contact velocity, and Δt is the time step.

The equation for translational motion is expressed as

$$F_i = m(\ddot{x}_{\mathrm{i}} - g_i), \tag{7}$$

where F_i is summation of all the externally applied forces acting on the particle, m is total mass of particle, $\ddot{x}_i$ is acceleration of particle, g_i is body force acceleration vector. The translational acceleration and rotational acceleration of particle can be calculated as

$$\ddot{x}_i^{(t)} = \frac{\dot{x}_i^{\left(t+\frac{\Delta t}{2}\right)} - \dot{x}_i^{\left(t-\frac{\Delta t}{2}\right)}}{\Delta t}, \tag{8}$$

$$\dot{\omega}_t^{(t)} = \frac{\omega_t^{\left(t+\frac{\Delta t}{2}\right)} - \omega_t^{\left(t-\frac{\Delta t}{2}\right)}}{\Delta t}. \tag{9}$$

where $\dot{x}_i$ is the translational velocity of the particle, and ω_t is the rotational velocity. The equation for rotational motion is expressed as

$$M_i = I\dot{\omega}_i, \tag{10}$$

where M_i is resultant moment acting on the particle, I is the moment of inertia of the particle and $\dot{\omega}_i$ is angular acceleration of the particle. The detailed theory for DEM can be found in Refs. [27–29].

2.3 Developed models for evaluation of hemisphere connection

The primary design parameters for the hemisphere connection are its diameter and embedment depth, as illustrated in Fig. 2 and detailed in Table 1. To determine appropriate dimensions, diameters of 800, 600, 400, and 200 mm were considered. For the depth, the exposed portion of the hemisphere was evaluated by applying embedment ratios of 3/3, 2/3, and 1/3 of the radius. The diameter has a direct impact on the shear resistance capacity, whereas the depth influences the relative movement performance of the connection between caissons, which in turn contributes to reducing stress concentration and promoting a more uniform distribution of wave forces along the breakwater.

2.4 Developed models for evaluation of embedded rebar connection within riprap connection

Continuous wave action in marine environments can cause stress concentration and fatigue failure at relatively vulnerable connections due to repeated loading. Therefore, to prevent stress concentration under moderate wave conditions with low external loads and to withstand

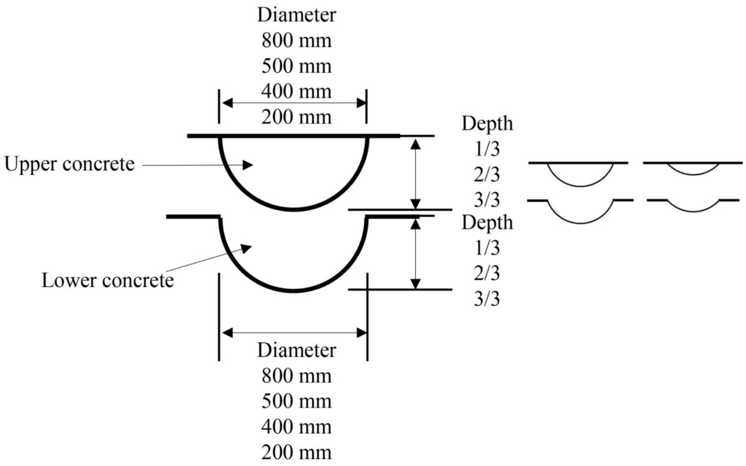

Fig. 2 Key parameters of hemisphere connection.

large waves generated by typhoons, the ERCR connection, as depicted in Fig. 3, was developed to dissipate wave forces while resisting them. The ERCR connection functions through the interlocking behavior of the riprap. Accordingly, the riprap size and void ratio were selected as the primary variables, as presented in Table 1 steel rebar is placed in each hole. In this study, the position of the rebar is ideally assumed to be centered within the hole. However, in practice, achieving perfect centering is difficult. Nevertheless, the repeated loading from wave action on the riprap is expected to influence the positioning of the riprap, allowing the rebar, though slightly deviated from the center—to behave similarly to one located at the center. This effect is especially relevant for cylindrical holes, where the rebar is not expected to significantly deviate from the central axis. When the rebar is embedded, stress concentration tends to occur at the connection, which is a structurally vulnerable region, particularly under repeated external loading in marine environments. To reduce this stress concentration, strategies such as increasing the cross-sectional area to improve stiffness may be adopted. Alternatively, permitting a certain degree of flexible behavior can help redirect the stress concentration from the caisson to the rebar. According to Lee et al. [19], such flexibility has been found to effectively redistribute stresses induced by external forces. The diameter of the rebars was also considered as a variable, as it is related to the shear resistance capacity. The diameters were selected relative to the typical size of riprap commonly used in South Korea, which is 250 mm. Thus, diameters of 150, 80, and 40 mm were chosen. The diameter of the rebar was also considered as a variable due to its relevance to shear resistance capacity. The selected diameters, 150, 80, and 40 mm—were determined relative to the typical riprap size used in South Korea, which is approximately 250 mm. The riprap size distribution was based on the study by Kim et al. [30], which compared actual riprap with discrete element-modeled riprap to more accurately simulate its behavior. According to this reference, the size distribution consists of 10.84% for the smallest size, 81.04% for the medium size, and 8.12% for the largest size. The corresponding diameters for each riprap category are listed in the "Diameter of riprap" column in Table 2. The model's name indicates the diameter of the rebar and the diameter of the riprap with the highest proportion in the distribution, allowing for clear identification of the key variables in each model. The proportions of the aggregates were determined based on the ratios commonly used for riprap in field applications. Specifically, the proportion of the largest-sized aggregate was set at 8.12%, the medium-sized aggregate at 81.04%, and the smallest-sized aggregate at 10.84%, with all proportions applied uniformly. For example, in the model named Rebar 0_40 mm, "Rebar 0" indicates that no rebar is used, while "40 mm" represents the most dominant riprap size category. Specifically, the Rebar 0_40 mm model refers to a case without rebar and is composed of riprap with diameters of 10–40, 40–55, and 55–65 mm, which account for 10.84%, 81.04%, and 8.12% of the overall distribution, respectively. The interaction between the rebar and riprap is modeled through contact, which can be observed in the deformation patterns and stress distributions of the rebar, as illustrated in Fig. 4. The riprap acts as a deformation-resistant medium while simultaneously offering lateral confinement to the internal rebar, effectively mitigating the risk of failure under excessive external loads.

The discrete elements used in this study are modeled as spherical particles, whereas actual riprap generally exhibits angular and irregular shapes. This difference in geometry presents limitations, particularly the inability of spherical elements to replicate the interlocking behavior characteristic of real riprap. In real conditions, riprap resists external forces not only through friction between individual stones but also through aggregate interlocking, which significantly enhances overall resistance. However, spherical discrete elements cannot reproduce this interlocking effect, resulting in reduced resistance and

Table 1 The scope of hemisphere connection

Parameter	Diameter (mm)	Embedded depth (depending on selected radius)
R100_D1/3	200	1/3
R100_D2/3	200	2/3
R100_D3/3	200	3/3
R200_D1/3	400	1/3
R200_D2/3	400	2/3
R200_D3/3	400	3/3
R400_D1/3	800	1/3
R400_D2/3	800	2/3
R400_D3/3	800	3/3

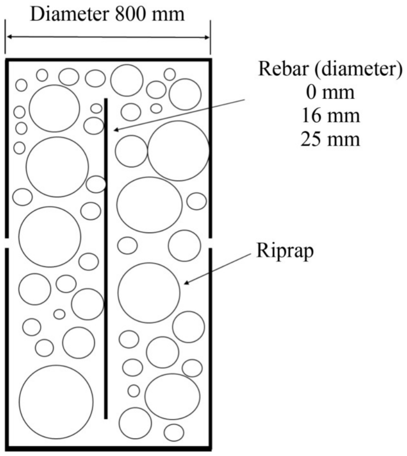

Fig. 3 Key parameters of ERCR connection.

Table 2 The scope of ERCR connection

Model name	Rebar diameter (mm)	Diameter of riprap by volume ratio (mm)		
		Volume ratio = 10.84%	Volume ratio = 81.04%	Volume ratio = 8.12%
Rebar 0_40 mm	no rebar	10–40	40–55	55–65
Rebar 0_60 mm	no rebar	15–60	60–83	83–93
Rebar 0_80 mm	no rebar	20–80	80–110	110–120
Rebar 0_100 mm	no rebar	25–100	100–140	140–150
Rebar 0_160 mm	no rebar	40–160	160–220	220–230
Rebar 16_40 mm	16	10–40	40–55	55–65
Rebar 16_60 mm	16	15–60	60–83	83–93
Rebar 16_80 mm	16	20–80	80–110	110–120
Rebar 16_100 mm	16	25–100	100–140	140–150
Rebar 16_160 mm	16	40–160	160–220	220–230
Rebar 25_40 mm	25	10–40	40–55	55–65
Rebar 25_60 mm	25	15–60	60–83	83–93
Rebar 25_80 mm	25	20–80	80–110	110–120
Rebar 25_100 mm	25	25–100	100–140	140–150
Rebar 25_160 mm	25	40–160	160–220	220–230

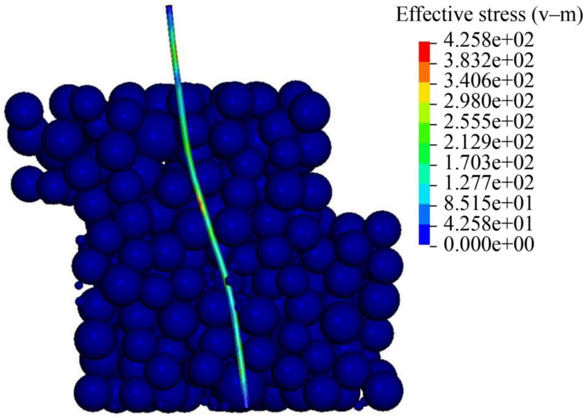

Fig. 4 The deformed shape of the rebar due to horizontal displacement (Rebar 16_40 mm).

mechanical behavior that deviates from that of actual riprap when standard friction coefficients are applied. To address this limitation, the friction coefficient was modified in this study to more accurately reflect the behavior of irregularly shaped riprap. Prior studies by Kim et al. [30], Lee [31], and Kragelski et al. [32] have shown that the friction coefficient is not constant, as it is influenced by frictional properties, interlocking characteristics, and adhesion at the contact interface. Based on these findings, the friction coefficients were adjusted accordingly. The rotational behavior between discrete elements was controlled by tuning both the sliding and rolling friction coefficients. Svanberg et al. [33] used a sliding friction coefficient of 0.9; in this study, a value of 1.0 was applied, as it was found to better replicate the mechanical behavior of irregular riprap. To ensure stable simulation, the rolling friction coefficient was set to 0.4. According to the Harbor and Fishery Design Criteria [34], the friction coefficient between concrete and riprap is 0.6. However, due to the constrained boundary conditions applied in this model, a higher friction coefficient was adopted for riprap. The shear friction coefficient was set to 1.0, and the final values used in the analysis are summarized in Table 3. As mentioned earlier, this was done to better represent the behavior of actual riprap by applying a higher value than the actual one. More detailed information on the selection of friction coefficients to simulate the behavior of riprap can be found in Kim et al. [30].

3 Structural evaluation using developed numerical model

This section presents a structural evaluation of the developed connection. The results from Section 3 were also applied in Section 4 to ultimately assess the stability of the structure against sliding and overturning.

Table 3 Selected frictional coefficients

Riprap to riprap		Concrete to riprap	
Sliding friction coefficient	Rolling friction coefficient	Normal friction coefficient	Shear friction coefficient
1.0	0.4	0.99	1.0

3.1 Development of structural evaluation model

The numerical model was constructed using solid elements and consists of an upper concrete block, a lower concrete block, and a rigid plate, as shown in Fig. 5(a). Contact interactions were defined using the contact function between the rigid plate and the upper concrete block, as well as between the upper and lower concrete blocks. The upper and lower concrete blocks were connected through the developed connection systems, illustrated in Figs. 5(b) and 5(c), and structural performance evaluations were conducted for each configuration. As mentioned in Subsection 2.1, the concrete was modeled using the CSCM model, which allows for the development of damage and failure. To evaluate the pure performance of the connection system, the lower concrete block was fully constrained to eliminate boundary effects. Nevertheless, in the final evaluation of structural performance, frictional shear resistance at the interface between the caisson and the seabed was incorporated to reflect realistic boundary conditions. All numerical analyses were performed using the LS-DYNA software. The evaluation procedure was carried out in two steps. In Step 1, only gravity was applied to simulate the load acting on the connection due to the self-weight of a single caisson unit. During this process, the buoyancy corresponding to mean sea level was also considered. In Step 2, displacement was gradually applied and controlled until failure occurred in the connection, enabling the assessment of structural performance under loading conditions.

3.2 Evaluation of hemisphere connection

In this study, the analysis was carried out using displacement control after the self-weight was applied to the entire structure. Figure 6 presents the plastic strain of the concrete as a function of displacement. Tensile strain occurs at the front in the direction of progression, while compressive strain develops at the rear.

The load–displacement graph is presented in Fig. 7. Upon analysis, it was observed that the maximum load for the hemisphere with a diameter of 200 mm and a depth of 3/3 (R100_D3/3) reached 7386 kN, representing a 355% increase compared to the maximum load of 1,625 kN for the same diameter with a depth of 1/3 (D100_D1/3). Similarly, for the 400 mm diameter case, the 3/3 depth model (R200_D3/3) exhibited a maximum load of 8942 kN, while the 1/3 depth model (D200_D1/3) showed 2547 kN, indicating a 251% increase. In the case of the 800 mm diameter model, the 3/3 depth configuration (R400_D3/3) recorded a maximum load of 12500 kN, compared to 6209 kN for the 1/3 depth model (D400_D1/3), resulting in a 101% increase. These results indicate that as the hemisphere diameter increases, the effect of embedment depth on the maximum load gradually diminishes. As also illustrated in Fig. 7, stiffness decreases with increasing displacement. This behavior is attributed to the displacement-controlled analysis method used in the evaluation. As displacement increases, the external force acting on the connection also increases, leading to progressive damage and eventual failure, which in turn causes a reduction in stiffness. In addition, the area under the load–displacement curve, indicative of ductile behavior, was clearly observed. After reaching the peak load, friction between the hemisphere and the contact surface allows the structure to sustain a certain level of load even at displacements up to 40–50 mm. This behavior suggests that the hemispherical

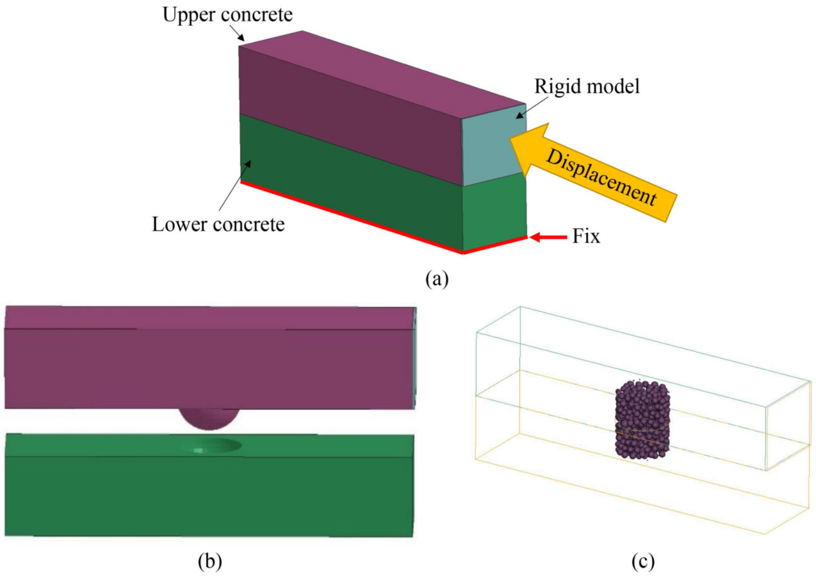

Fig. 5 Developed numerical model of novel connection systems: (a) developed numerical model; (b) hemisphere connection; (c) ERCR connection.

connection permits minor sliding, which enables the absorption of shock and alleviates stress concentration at the joint.

Figures 8(a) and 8(b) present the relationship between load and diameter, and load and contact area, respectively. As shown in Fig. 8(a), an increase in diameter leads to a nearly linear improvement in shear resistance performance. When considering diameter alone, without accounting for depth, it was found that each 1 mm increase in diameter corresponds to an average increase of approximately 9.3 kN in maximum load. To consider geometric effects more accurately, the

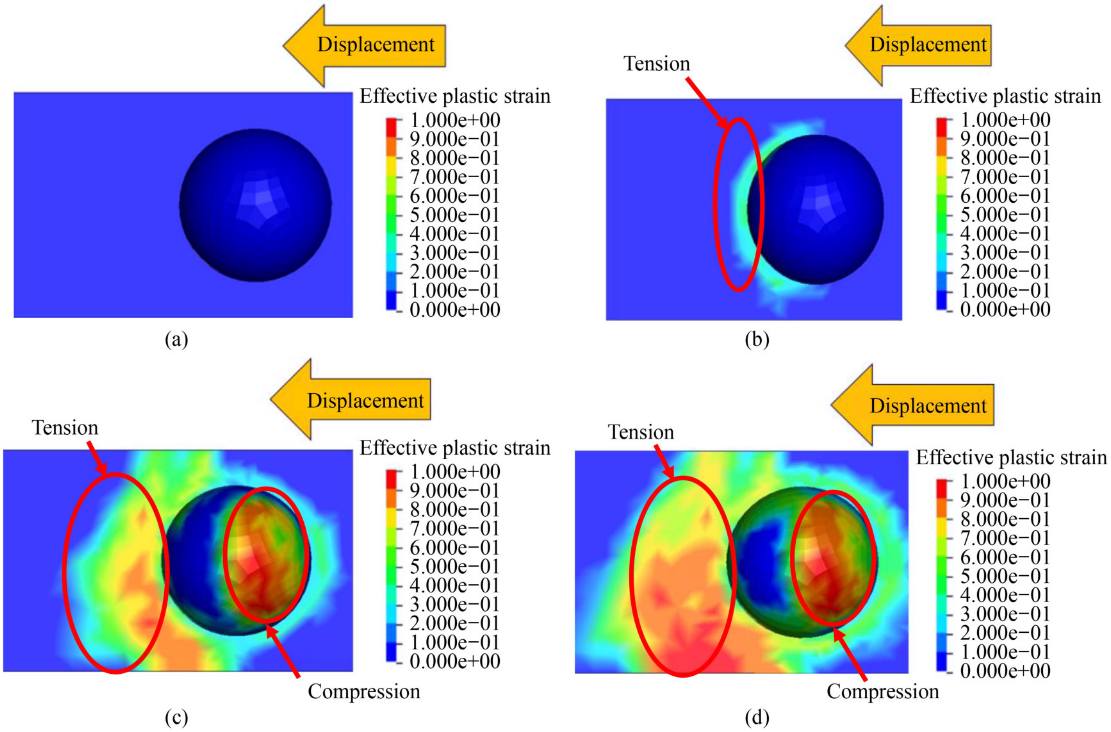

(a) (b) (c) (d)

Fig. 6 Plastic strain contour due to horizontal displacement (diameter 800 mm, depth 3/3): (a) 0 mm; (b) 5 mm; (c) 10 mm; (d) 20 mm.

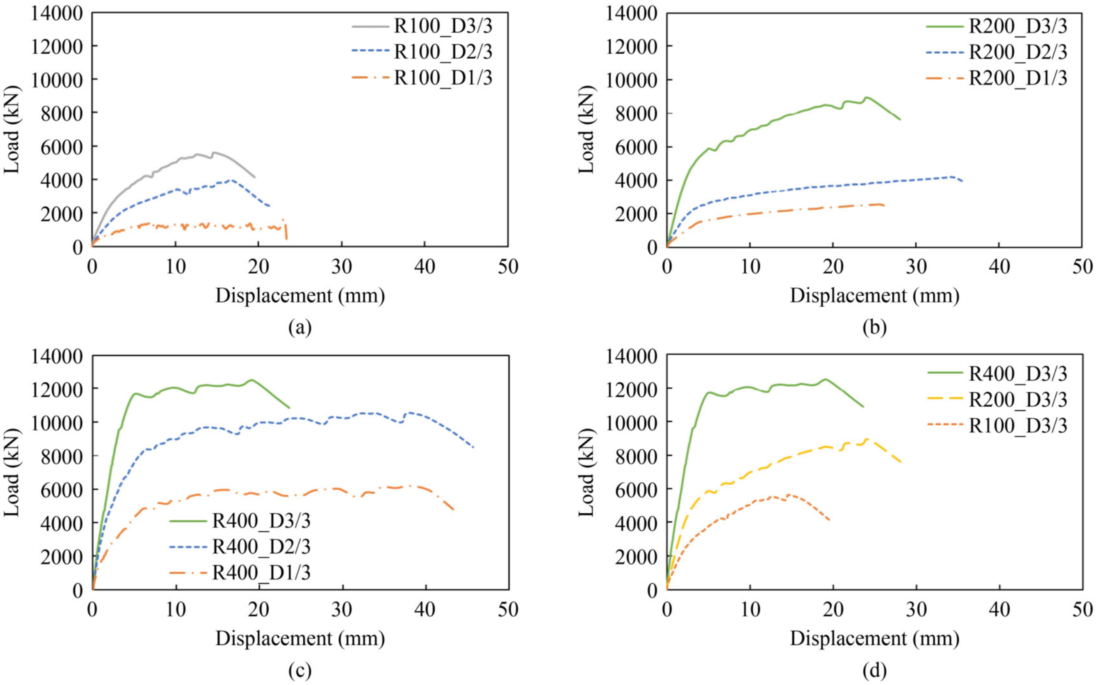

(a) (b) (c) (d)

Fig. 7 Load–displacement graph of hemisphere connection: (a) diameter 200 mm; (b) diameter 400 mm; (c) diameter 800 mm; (d) depth 3/3.

load was also analyzed as a function of contact area, as shown in Fig. 8(b). The results confirm that the maximum load increases with increasing contact area. Specifically, a 0.1 m^2 increase in contact area corresponds to an approximate increase of 939 kN in maximum load.

Figure 9 illustrates the energy absorbed by the hemisphere connection, calculated as the area under the load–displacement curves presented in Fig. 7. As shown in Fig. 9(a), the absorbed energy generally increases with increasing diameter, as expected. However, for a diameter of 800 mm, the energy absorbed at a depth of 3/3 was 257 kJ, whereas at a depth of 2/3 it reached 419 kJ, representing a 63% increase in energy absorption efficiency at the 2/3 depth compared to the 3/3 depth. This result suggests that, although the 3/3 depth exhibits a higher maximum load, as seen in Fig. 7(c), it does not necessarily correspond to greater energy absorption. This phenomenon is attributed to more severe stress concentration at the constrained boundary in the 3/3 depth condition. In contrast, the 2/3 depth reduces stress concentration, making it more effective for energy dissipation. Therefore, configurations such as the 2/3 depth, which induce lower stress concentration, are more favorable for improving energy absorption than full hemisphere shapes. Figure 9(b) further shows that the absorbed energy increases by approximately 29 kJ for every 0.1 m^2 increase in contact area. These findings indicate that while increasing depth enhances load resistance, the 2/3 depth provides better energy absorption characteristics. Accordingly, it is necessary to identify an optimal balance between maximum load capacity and energy absorption, and to reflect this balance in the design process.

3.3 Evaluation of embedded rebar connection within riprap connection

The load–displacement graph of the ERCR connection under displacement, as confirmed through the analysis, are shown in Figs. 10–12. Comparing Fig. 10(a) with Figs. 10(b)–10(d), during the initial stage of displacement, the voids in the riprap decreased. This is due to the no compaction performed after the initial installation of the riprap. As additional displacement occurs, the rebar also resists and supports the movement, playing a crucial role in limiting excessive displacement.

Figure 11 presents the load–displacement results for the following cases: (a) without rebar, (b) and (c) with rebars of different diameters, and (d) with rebars of varying diameters applied to riprap of the same size (40 mm). The wavy pattern observed in the load–displacement curves is attributed to the behavior of the riprap under external loading. When subjected to load, the riprap not only resists the force but also undergoes slight movement, resulting in fluctuations in the resistance force. As shown in Fig. 11, larger riprap diameters generally exhibited

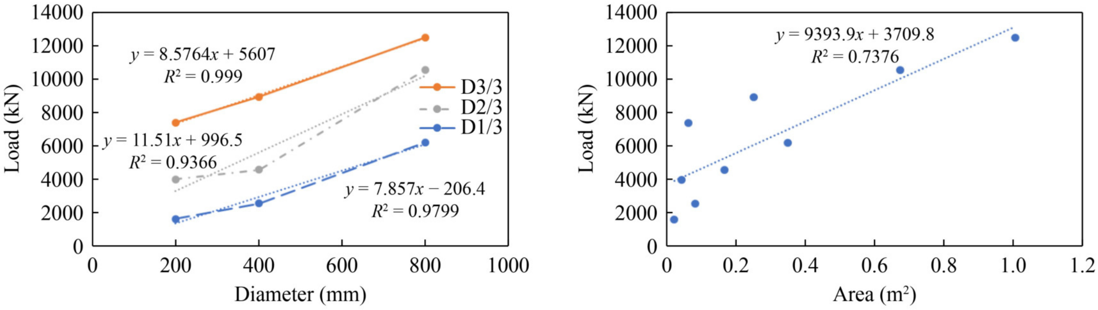

(a) (b)

Fig. 8 Load–displacement curve depending on diameter and area of hemisphere connection: (a) load versus diameter graph; (b) load versus area graph.

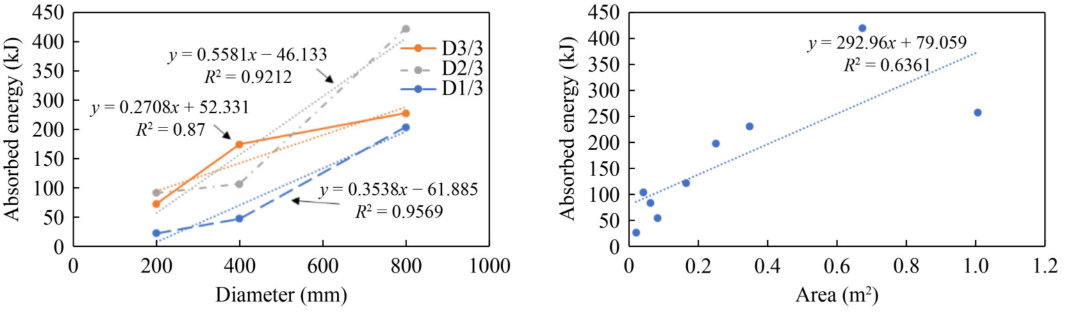

(a) (b)

Fig. 9 Energy absorption depending on hemisphere size: (a) energy absorption depending on hemisphere connection diameter; (b) energy absorption depending on hemisphere area.

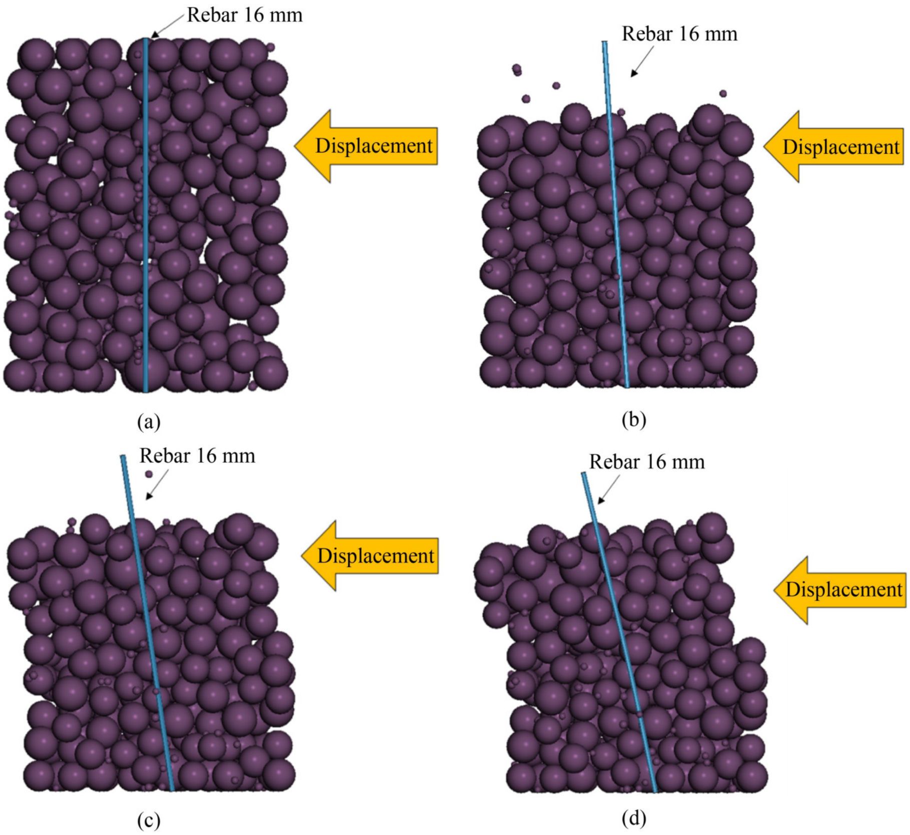

Fig. 10 Deformed shape of riprap with rebar of 16 mm diameter: (a) horizontal displacement 0 mm; (b) horizontal displacement 10 mm; (c) horizontal displacement 50 mm; (d) horizontal displacement 100 mm.

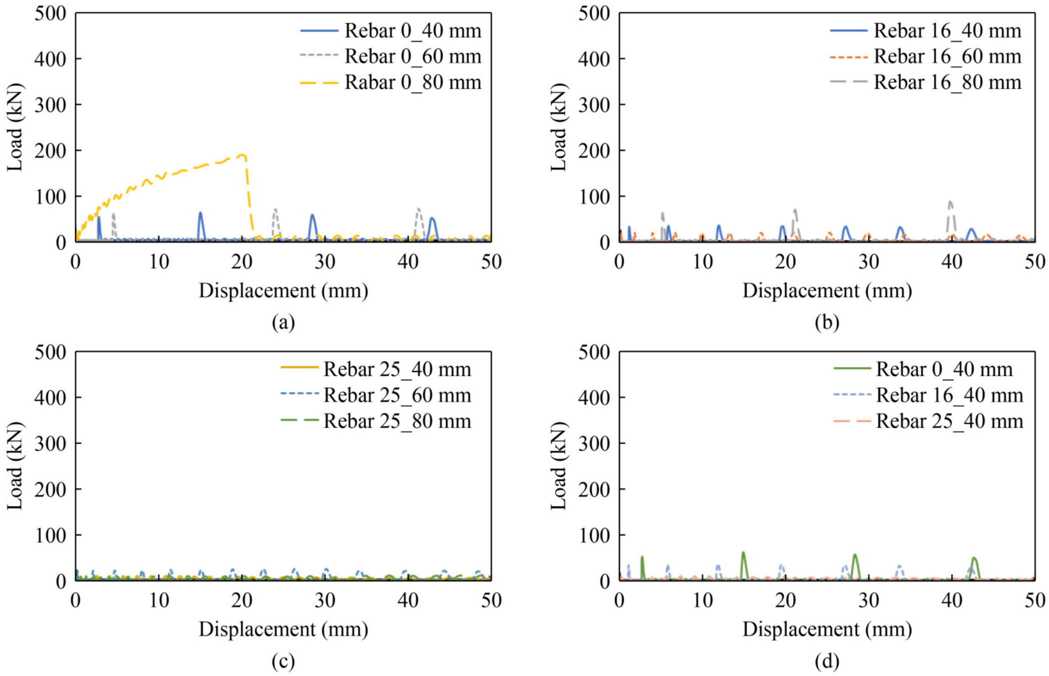

Fig. 11 Load–displacement graph of ERCR connection: (a) Rebar 0; (b) Rebar 16; (c) Rebar 25; (d) riprap size (40 mm).

relatively improved structural performance. However, the improvement in resistance was not significant. In particular, for case (d), where different rebar diameters were applied to the same riprap size, no notable enhancement in performance was observed. On the contrary, the configuration without rebar demonstrated slightly higher resistance. This result is attributed to the assumption in the current study that the riprap particles are spherical, which does not adequately capture the interlocking behavior characteristic of actual riprap. Consequently, the presence of rebar may have interfered with the riprap movement, rather than contributing to improved resistance.

In the ERCR connection, the riprap was arranged based on the predefined size ratio, which resulted in incomplete filling and the presence of voids within the connection. Rather than eliminating voids through compaction, the riprap was placed according to its intended size distribution, leading to the formation of gaps between individual particles. During the analysis, these gaps caused the riprap to be rearranged under the influence of gravity. As shown in Fig. 12, the riprap settled downward and redistributed, creating a void space at the top of the connection. As a result, contrary to the initial expectation that the riprap would resist external forces through inter-particle friction, the upper void allowed the riprap to shift upward into the empty space, thereby failing to provide sufficient resistance against wave forces. This behavior is attributed to the lack of constraint from above. It was also observed that smaller riprap diameters resulted in smaller void spaces, while larger particles contributed to more significant gaps. The presence of rebar was also expected to improve structural performance by interacting with the riprap. However, the analysis revealed that the riprap did not adequately restrain the rebar. As shown in Fig. 13, the embedded rebar was not sufficiently confined, causing it to tilt in the direction of the applied force. This movement interfered with the resistance capacity of the surrounding riprap, ultimately creating more voids and reducing the overall structural performance compared to the case without rebar. Additionally, as the diameter of the rebar increased, structural performance further declined. These results are likely due to the absence of compaction and the unrestrained space at the top of the connection. Therefore, to enhance the effectiveness of the ERCR connection, proper compaction must be applied during installation, and the riprap should be sufficiently constrained from above.

Since the actual ERCR connection is intended to have no void space between the riprap and the upper concrete,

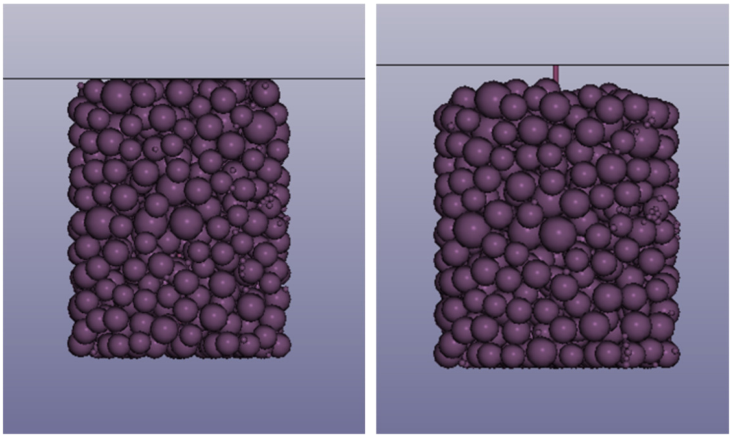
(a) (b)

Fig. 12 Formation of void space due to gravity: (a) before the action of gravity; (b) after the action of gravity.

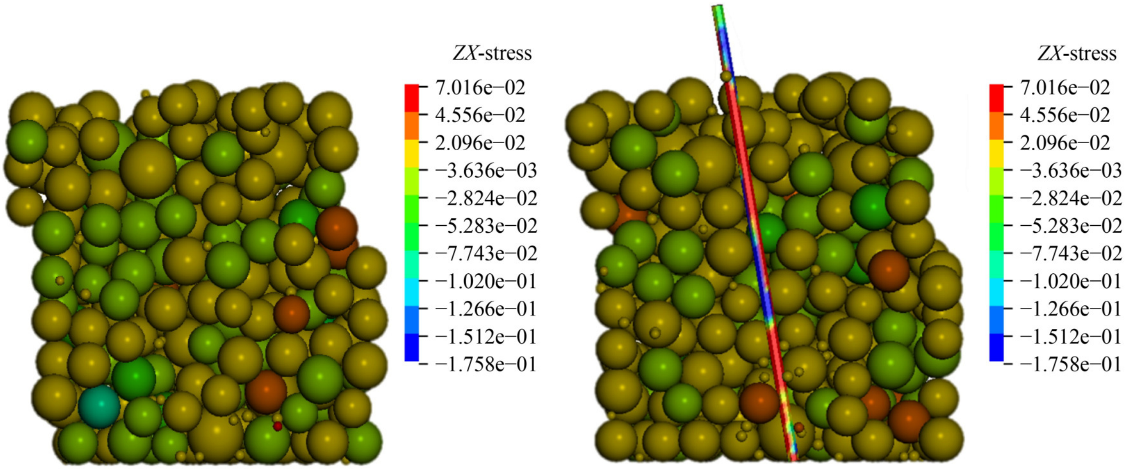

(a) (b)

Fig. 13 Stress contour (*ZX*-axis): (a) Rebar 0_40 mm; (b) Rebar 25_40 mm.

a plate, assumed to be in contact only with the riprap—was introduced and moved downward along the *Z*-axis to reduce the void space formed by the redistribution of the riprap due to gravity, as shown in Fig. 14. The friction between the plate and the riprap was modeled using the same friction coefficient applied between the riprap and the upper concrete, assuming direct contact. Figure 15 presents the load–displacement results for the case in which the plate was lowered to eliminate the void space at the top of the riprap. Across all riprap sizes, it was observed that reducing the upper void space improved structural performance compared to the case without void reduction, as shown in Fig. 11. In this study, the configuration with the lowered plate is labeled as "full" in the figures. As expected, the structural performance of the ERCR connection improved as the riprap size decreased, confirming that the presence of void space in the riprap section has a significant effect on overall behavior. In Fig. 15(d), it is also shown that increasing the rebar diameter tends to decrease structural performance. To further investigate the influence of rebar diameter on ERCR performance, an additional analysis was conducted by applying boundary constraints to the rebar. Specifically, the bottom surface of the rebar was fixed to the lower concrete block, and the simulation was performed under this condition. This fixed-rebar configuration is labeled as "fix" in Fig. 16. As illustrated in Fig. 16, structural performance was improved in all cases when the rebar was constrained, compared to when it was left unrestrained. Furthermore, Fig. 16(c) clearly

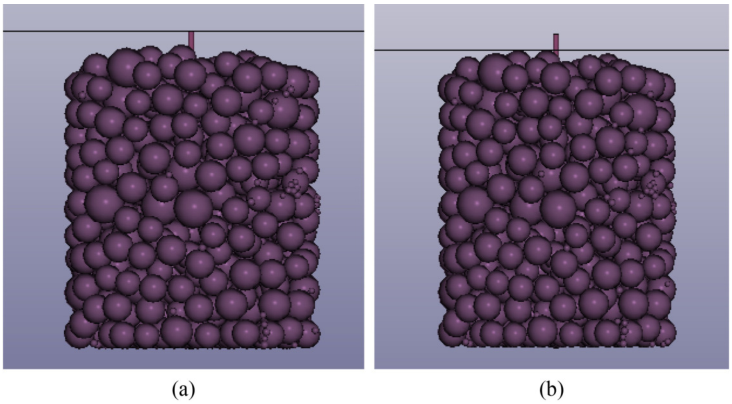

Fig. 14 The lowered plate to reduce the void space: (a) original plate location; (b) lowered plate location.

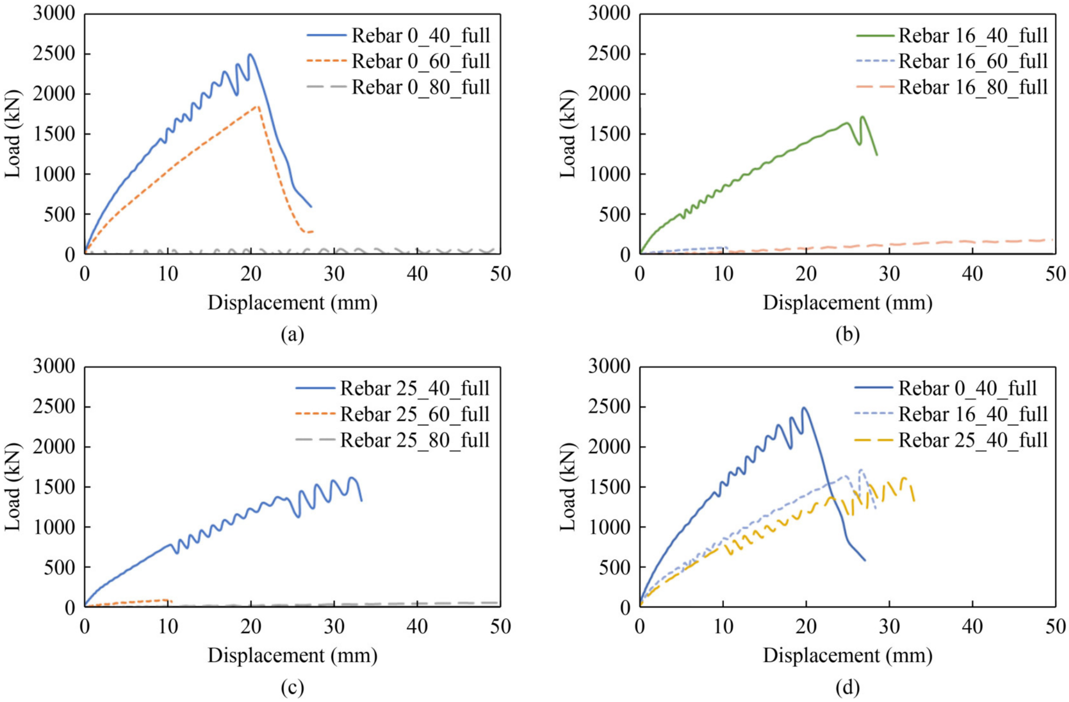

Fig. 15 Load–displacement graph of ERCR connection after lowering the top plate: (a) Rebar 0; (b) Rebar 16; (c) Rebar 25; (d) riprap diameter 40 mm.

shows that sufficient constraint on the rebar enhances the structural performance of the ERCR connection. As the voids between the riprap decrease and the contact with the rebar increases, a greater portion of the load is transferred to the rebar. This indicates that stress concentration, which would typically occur at structurally vulnerable locations, becomes more focused on the rebar. However, this effect is only meaningful when the rebar is sufficiently constrained. The results confirm that the structural performance of the ERCR connection is significantly affected by whether or not the rebar is properly restrained. Furthermore, when comparing structural performance based on rebar diameter, it was found, contrary to initial expectations—that the smaller 16 mm rebar provided better performance than larger diameters. As illustrated in Figs. 17(a) and 17(b) illustrate that while the 16 mm rebar undergoes noticeable bending under external forces, the 25 mm rebar exhibits lower deformation under the same loading conditions, indicating reduced susceptibility to external forces. Additionally, Fig. 17(c) shows that the 16 mm rebar absorbed more internal energy than the 25 mm rebar. This suggests that the flexible behavior of the 16 mm rebar contributes to greater energy absorption, resulting in improved structural performance. These findings indicate that enhancing wave resistance through energy absorption and ductile behavior may be more effective than relying solely on increased stiffness. However, due to the continuous nature of wave loading in marine environments, it is essential to consider the allowable displacement limits. Therefore, the optimal combination of parameters, such as rebar diameter, aggregate size, and hole dimensions—must be carefully selected. Future research will aim to identify and optimize these design parameters to further improve the performance of the ERCR connection.

The analysis results confirm that as the void space within the riprap is more effectively reduced, the performance of the ERCR connection tends to improve. In cases where the riprap fails to provide adequate restraint to the rebar, the structural performance decreases. Conversely, when the riprap sufficiently confines the rebar, the performance of the ERCR connection improves. It is assumed that in actual applications of the ERCR system, proper compaction will minimize voids within the riprap layer, thereby enabling sufficient confinement of the rebar. Figure 18(a) illustrates the energy absorption of the ERCR connection as a function of riprap diameter. The results indicate that energy absorption increases with larger riprap sizes. However, the analysis also confirms that an optimal combination of rebar diameter and riprap diameter is necessary to achieve maximum energy absorption efficiency. Figure 18(b) compares energy absorption based on whether the rebar is confined. When the rebar is fully restrained, the absorbed energy increases by up to 13191%, demonstrating that rebar confinement has a significant influence on the performance of the ERCR connection. Nevertheless, the energy absorption of the ERCR connection remains considerably lower than that

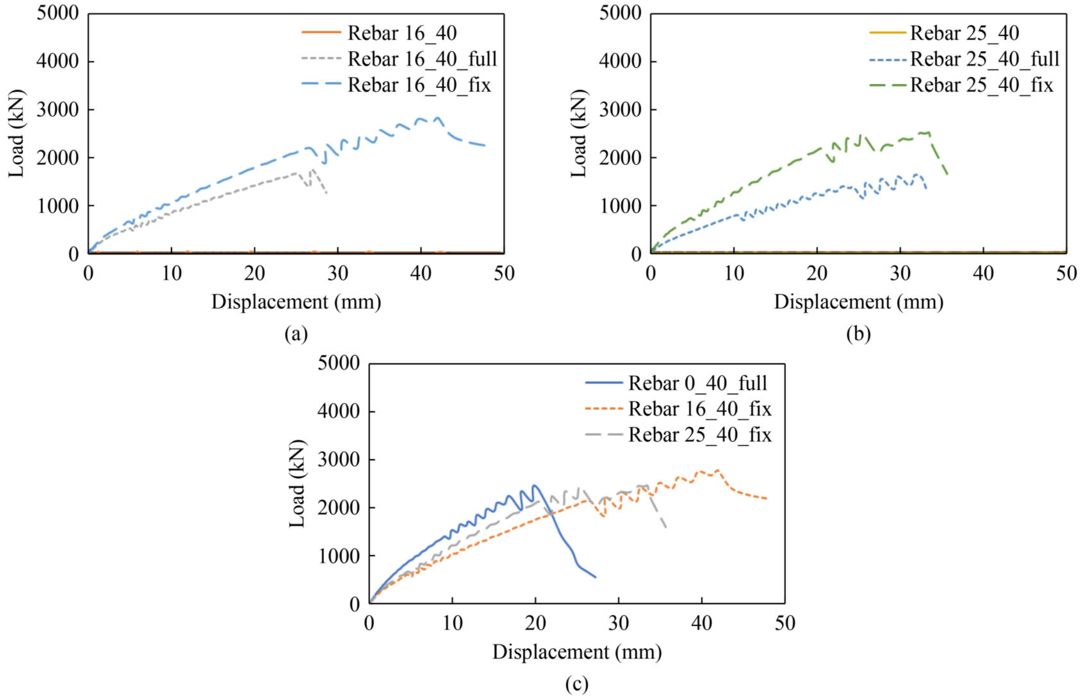

(a)

(b)

(c)

Fig. 16 Comparison of load–displacement graph of ERCR connection after rebar fixed: (a) Rebar 16; (b) Rebar 25; (c) riprap diameter 40 mm.

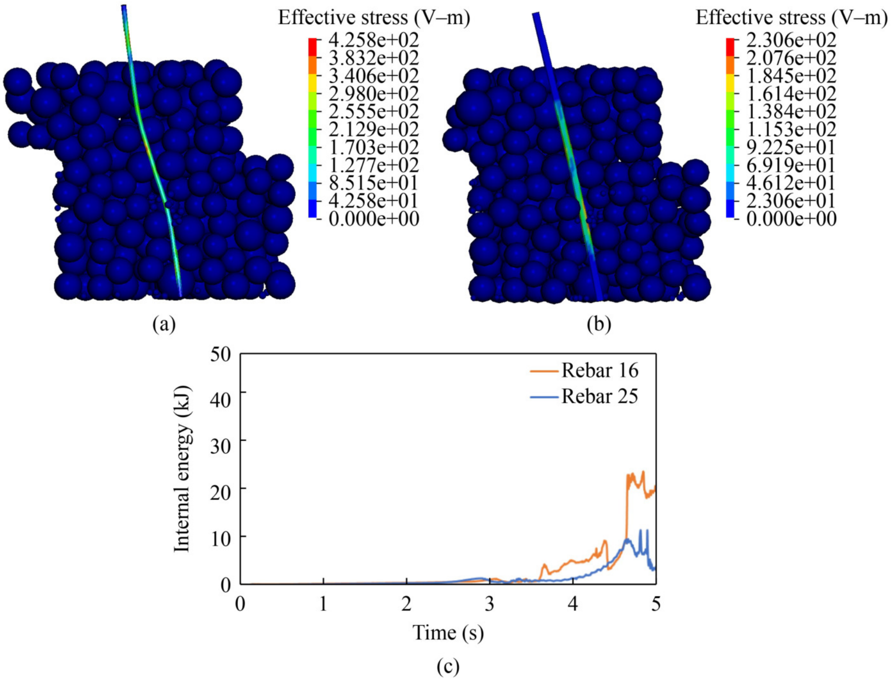

Fig. 17 Rebar after the application of external forces: (a) Rebar 16_40 mm; (b) Rebar 25_40 mm; (c) internal energy.

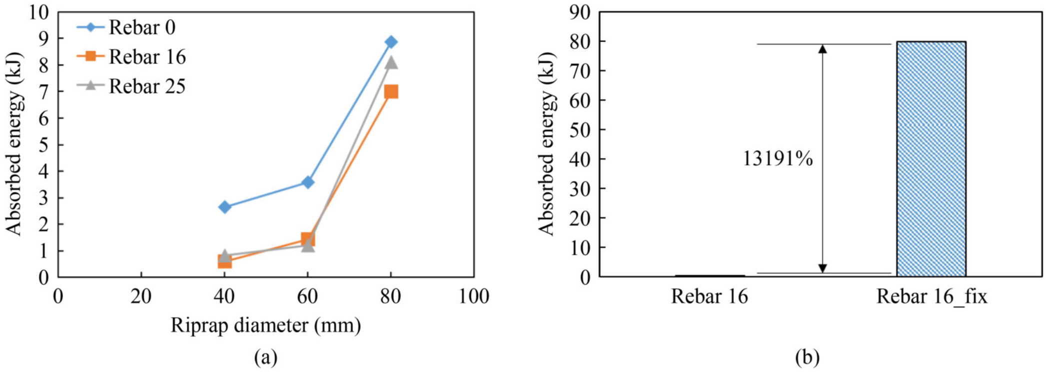

Fig. 18 Energy absorption of ERCR connection: (a) energy absorption versus riprap diameter; (b) energy absorption of Rebar 16_fix (riprap diameter 40 mm).

of the hemisphere connection, primarily due to its lower stiffness. Based on these findings, it is suggested that the hemisphere connection is more suitable for application in outer sea conditions, where it can more effectively distribute wave loads among adjacent caissons. In contrast, the developed ERCR connection is considered more appropriate for use in inner sea conditions, where wave forces are relatively moderate and controlled displacement can be beneficial for energy dissipation.

4 Stability evaluation of developed caisson

In this section, the performance of the hemisphere connection and the ERCR connection, as described in Section 3, was applied to a full-scale breakwater consisting of multiple caissons. The enhanced stability of these structures, against sliding and overturning, was evaluated under wave forces due to the effects of the developed novel connection systems.

4.1 Wave condition

A case study was conducted to examine the developed connections under real marine wave load conditions, considering the actual weight of the breakwater. Although the study by Moghadam et al. [35] has been conducted on estimating wave forces acting on caissons, the present study focuses on evaluating the developed connection. Therefore, a more conservative approach was adopted by using the wave pressure values calculated based on Goda’s formula. The wave force was calculated based on the conditions off the coast of Pohang, South Korea, where the water depth, wave height, and period are 18 m, 7.7 m, and 11 s, respectively. The incident angle was set to 30°. The wave force acting on the structures under marine conditions must consider the phase difference. The equation considering the phase difference of the wave force is as follows:

$$F_{\mathrm{H}}^{\mathrm{W}} = F_{\mathrm{H}}^{\mathrm{G}} \times \gamma_{\mathrm{d}}, \tag{11}$$

$$F_{\mathrm{V}}^{\mathrm{W}} = F_{\mathrm{V}}^{\mathrm{G}} \times \gamma_{\mathrm{d}}, \tag{12}$$

$$\gamma_{\mathrm{d}} = \gamma \cos\delta, \tag{13}$$

$$\delta = k y_i \sin\varphi, \tag{14}$$

$$\gamma = \frac{\sin \dfrac{k W_{\mathrm{c}} \sin\varphi}{2}}{\dfrac{k W_{\mathrm{c}} \sin\varphi}{2}}, \tag{15}$$

where $F_{\mathrm{H}}^{\mathrm{W}}$ is the horizontal design wave force, $F_{\mathrm{V}}^{\mathrm{W}}$ is the vertical design wave force, $F_{\mathrm{H}}^{\mathrm{G}}$ and $F_{\mathrm{V}}^{\mathrm{G}}$ are the horizontal and vertical wave forces based on Goda's wave pressure [36], respectively, γ_{d} is the reduction factor considering the phase difference, k is wave number , y_i is the center-to-center distance from the first to the ith connected caisson, φ is the incident wave angle, γ is the phase difference of the in-plane pressure, and W_{c} is the width of a single caisson. Detailed information on wave force calculation can be found in Ref. [37]. Using this equation, both positive and negative wave force values were obtained. Figure 19 presents the calculated wave force. The negative values represent forces acting in the opposite direction, which tend to drive the structure seaward. Since this phenomenon differs under actual conditions, negative values were set to zero in the wave force applied to the analysis model. In the stability evaluation model, wave pressure was applied to the nodes rather than the surface of the caisson. Figure 19 illustrates the wave pressure used in the analysis. The force acting on a single caisson is presented, with a time delay incorporated into the loading on the structure to account for the incident angle of the waves. For this analysis, an incident angle of 30°, a wave period of 11 s, a water depth of 18 m, and a wave height of 7.7 m were selected, based on the wave conditions off the coast of Pohang. Although the attenuation of wave force with depth due to fluid viscosity was not considered, the total wave force acting on a caisson was uniformly distributed across the nodes extending from the seabed to the mean sea level. This simplified yet conservative modeling approach was adopted to assess the performance of the proposed connection systems under intensified wave conditions. Detailed results of numerical analysis are shown in Subsection 4.3.

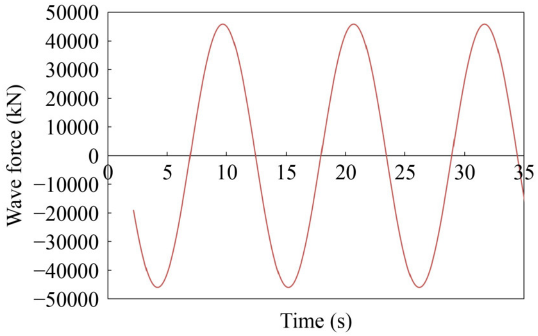

Fig. 19 Wave force applied to FE model.

4.2 Model development of stability evaluation

The performance of the developed connection systems was evaluated by applying them to a full-scale three-dimensional (3D) model to assess their effectiveness under wave loading. The dimensions of a single caisson unit were defined as 23449 mm in height, 21000 mm in width, and 28700 mm in length. The weight of a single caisson was calculated by considering the combined mass of the rubble mound, concrete, and internal voids. Assuming a configuration of nine consecutive caissons, the total length of the breakwater was determined to be 258306 mm. The frictional force between the seabed and the lower surface of the caisson was modeled using a friction coefficient of 0.6, as specified in the Harbor and Fishery Design Standards (KDS 64 10 10) [34]. Additionally, the frictional force between adjacent caissons was calculated by applying a friction coefficient of 0.5, representing the concrete-to-concrete interface (KDS 14 20 20) [38]. The novel connection systems developed in this study were implemented to continuously link adjacent caissons. These connections were modeled using spring elements, with their load–displacement properties derived from the analysis results presented in Section 3, as shown in Fig. 20. To simplify the model, the caisson geometry was idealized as a hexahedron. This simplified model accounted for the equivalent self-weight, including internal voids, as well as the buoyant force resulting from submersion in seawater. Wave forces were modeled by treating the caisson as a single mass module, with the forces applied at the caisson's centroid. It was assumed that these forces acted on all nodes extending from the seabed to the mean sea level at the center of the caisson.

4.3 Evaluation of stability of long caisson with developed novel connections

Figure 21 illustrates the lateral sliding behavior of the caissons under wave loading. Compared to the conventional caisson without a novel connecting system

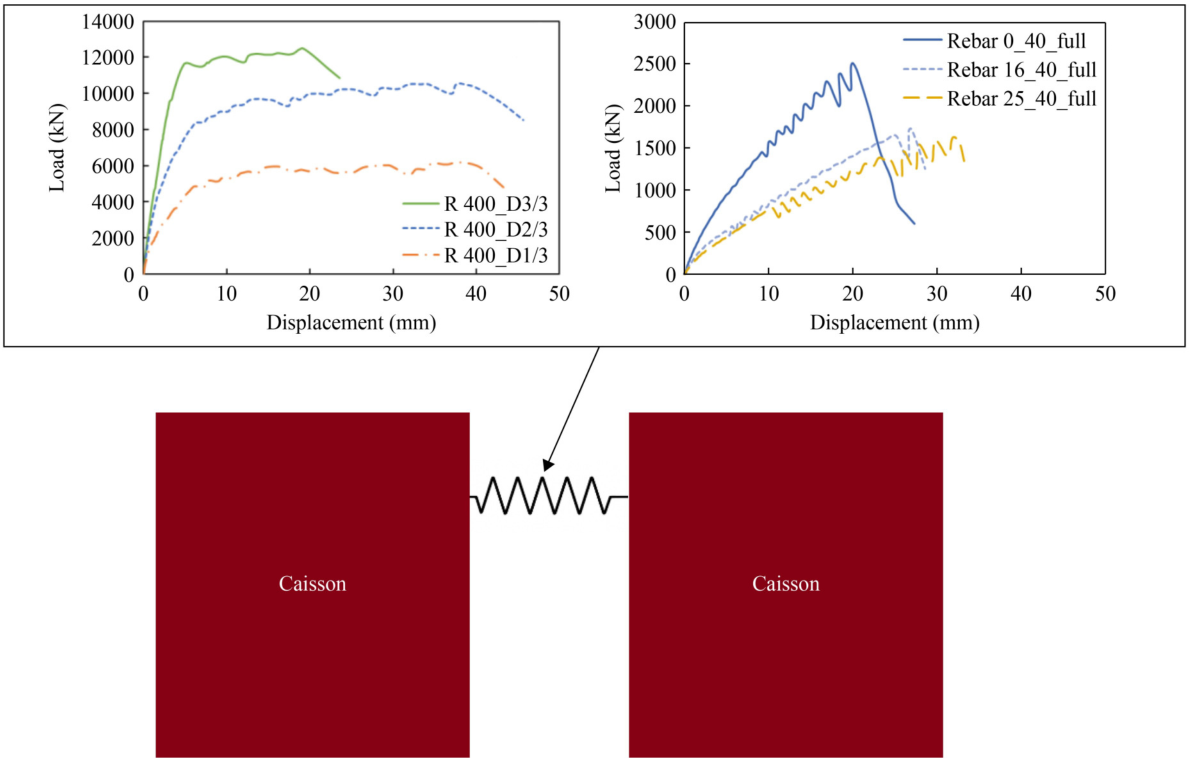

Fig. 20 Nonlinear spring elements used to represent novel connection systems

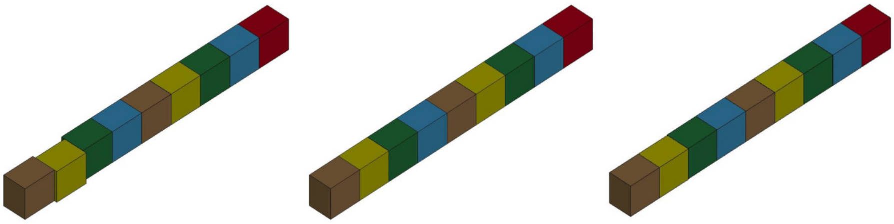

(a) (b) (c)

Fig. 21 Stability results of developed numerical model: (a) conventional caisson isometric view (no connection); (b) hemisphere connection caisson isometric view (diameter 800 mm, depth 3/3); (c) ERCR connection caisson isometric view (Rebar 16_fix riprap diameter 40 mm).

(Fig. 21(a)), the caissons with the hemisphere connection (Fig. 21(b)) and the ERCR connection (Fig. 21(c)) exhibit significantly reduced lateral sliding displacement. In the absence of a novel connecting system, the conventional caisson experienced a maximum lateral sliding displacement of approximately 1.6 m. Among these, the hemisphere connection with a diameter of 800 mm and a depth of 3/3 showed the least displacement, reducing movement by up to 99% compared to the conventional case. A similar reduction was also observed with the ERCR connection at a depth of 2/3, which significantly reduced displacement compared to the unconnected configuration. These results demonstrate that the proposed hemisphere and ERCR connection systems effectively enhance wave load resistance and improve the overall stability of individual caissons in long breakwater structures. Future research should include experimental validation of the developed connections and field-scale testing to assess practical applicability. In addition, the fatigue performance of the connection systems under cyclic wave loading must be evaluated.

5 Conclusions

This study evaluated the structural performance of newly developed novel connection systems (the hemisphere and ERCR) for elongated breakwaters consisting of multiple laterally connected precast caissons subjected to wave loading. The main conclusions are summarized as follows.

1) When considering only the diameter of the hemisphere connection without accounting for embedment depth, the maximum load resistance was found to increase by approximately 9.3 kN for every 1 mm increase in diameter. Additionally, a 0.1 m^2 increase in

the contact area of the hemisphere connection resulted in an approximate increase of 939 kN in maximum load resistance.

2) The performance evaluation of the hemisphere connection indicated that for a diameter of 800 mm, the energy absorbed was 257 kJ at a depth of 3/3 and 419 kJ at a depth of 2/3, representing a 63% increase in energy absorption at the 2/3 depth compared to the 3/3 depth. These results suggest the importance of considering both maximum load capacity and energy absorption in the design process. Accordingly, it is necessary to propose an appropriate embedment depth for each diameter to satisfy design objectives related to load resistance and energy dissipation.

3) The performance of the ERCR connection is significantly affected by the confinement of the rebar and the compaction condition of the riprap. Analysis results showed that the 16 mm rebar absorbed more energy than the 25 mm rebar, as the latter was less effective due to its limited ability to deform under external forces. These findings highlight the importance of selecting an appropriate combination of rebar diameter and riprap size to achieve optimal energy absorption under wave loading conditions.

4) The findings suggest that enhancing wave resistance through energy absorption and ductile behavior is more effective than relying solely on the high stiffness of the connection system.

5) The stability evaluation of long caissons incorporating the developed novel connections demonstrated that these systems can be effectively applied at relatively low cost, significantly reducing the risk of sloping failure and other structural issues in breakwaters. Under identical wave conditions, caissons with the proposed connections exhibited up to a 99% reduction in sliding compared to conventional caissons without interconnection.

Future research will focus on assessing the structural behavior of rebar-only configurations, excluding the use of riprap, to isolate the contribution of the reinforcing elements.

Based on the numerical findings presented in this study, a detailed design phase is currently in progress. Final validation of the proposed connection systems will be conducted through a 3D wave flume experiment to ensure the accuracy and applicability of the numerical modeling assumptions.

Acknowledgements This research was supported by Basic Science Research Program through the National Research Foundation of Korea (NRF) funded by the Ministry of Education (Nos. RS-2023-00212586 and RS-2024-00348557) and the Korea Maritime & Ocean University Research Fund in 2024.

Competing interests The authors declare that they have no competing interests.

References

1. Takayama T, Higashira K. Statistical analysis on damage characteristics of breakwaters. Proceedings of Civil Engineering in the Ocean, 2002, 18: 263–268
2. Chaudhary B, Hazarika H, Murakami A, Fujisawa K. Countermeasures for enhancing the stability of composite breakwater under earthquake and subsequent tsunami. Acta Geotechnica, 2018, 13(4): 997–1017
3. Chaudhary B, Hazarika H. Centrifuge modelling for stability evaluation of a breakwater foundation subjected to an earthquake and a tsunami. Ocean Engineering, 2018, 148: 169–181
4. Chaudhary B, Hazarika H, Murakami A, Fujisawa K. Mitigation of earthquake induced damage of breakwater by geogrid reinforced foundation. Marine Georesources and Geotechnology, 2018, 36(7): 827–840
5. Chaudhary B, Hazarika H, Nishimura N. Effects of duration and acceleration level of earthquake ground motion on the behavior of unreinforced and reinforced breakwater foundation. Soil Dynamics and Earthquake Engineering, 2017, 98: 24–37
6. Chaudhary B, Hazarika H, Ishibashi I, Abdullah A. Sliding and overturning stability of breakwater under combined effect of earthquake and tsunami. Ocean Engineering, 2017, 136: 106–116
7. Chaudhary B, Hazarika H, Pasha S M K. Countermeasures for breakwater foundation subjected to foreshocks and main shock of earthquake loading. Marine Georesources and Geotechnology, 2018, 36(3): 308–322
8. Chaudhary B, Hazarika H, Nishimura N. Effects of reinforcement on the performance of breakwater foundation subjected to earthquake loadings. International Journal of Geotechnical Engineering, 2016, 11(2): 186–197
9. Mimura N. Sea-level rise caused by climate change and its implications for society. Proceedings of the Japan Academy. Series B, Physical and Biological Sciences, 2013, 89(7): 281–301
10. Takahashi S, Shimosako K. Reduction of Wave Force on a Long Caisson of Vertical Breakwater and Its Stability. Technical Notes. 1990, 685
11. Park W S, Won D, Seo J, Lee B W. Proposal of rotating stability assessment formula for an interlocking caisson breakwater subjected to wave forces. Journal of Korean Society of Coastal and Ocean Engineers, 2020, 32(1): 11–16
12. Seo J, Won D, Park W S. Behavior of walls of open-cell caissons using filler under abnormally high waves. Journal of Korean Society of Coastal and Ocean Engineers, 2017, 29(2): 83–91
13. Lee BW, Won D, Kim DH, Park WS. Model tests for evaluating the bearing pressure of harbor structures using open cell caisson method. Journal of Coastal Research, 2021, 114(SI): 26–30
14. Seo J, Won D, Park W. Behavior of inter-cell for open-cell caisson breakwater system. In: CODE 2018. Seoul: Computational Structural Engineering Institute of Korea (COSEIK), 2018, 328
15. Kim W, Lee I, Kim K, Jeong Y, Lee J. Evaluation of concrete barriers with novel shock absorbers subjected to impact loading. Archives of Civil and Mechanical Engineering, 2019, 19(3): 657–671
16. Kim W, Lee I, Jeong Y, Zi G, Kim K, Lee J. Design approach for

improving current concrete median barriers on highways in South Korea. Journal of Performance of Constructed Facilities, 2018, 32(3): 04018022

17. Murray D Y. Users Manual for LS-DYNA Concrete Material Model 159. United States: Federal Highway Administration, Office of Research, Development, and Technology, 2007
18. Lee J, Zi G, Lee I, Jeong Y, Kim K, Kim W. Numerical simulation on concrete median barrier for reducing concrete fragment under harsh impact loading of a 25-ton truck. Journal of Engineering Materials and Technology, 2017, 139(2): 021015
19. Lee J, Jeong Y, Kim K, Lee I, Kim W. Experimental and numerical investigation of deformable concrete median barrier. Materials, 2019, 12(19): 3176
20. Kim K, Kim W, Seo J, Jeong Y, Lee J. The amount prediction of concrete fragments after impact using smoothed particle hydrodynamics. Engineering Failure Analysis, 2022, 131: 105882
21. Kim K, Kim W, Seo J, Jeong Y, Lee J. Quantitative measure of concrete fragment using ANN to consider uncertainties under impact loading. Scientific Reports, 2022, 12(1): 11248
22. Murray D Y, Abu-Odeh A, Bligh R. Evaluation of LS-DYNA Concrete Material Model 159. United States: Federal Highway Administration, Office of Research, Development, and Technology, 2007
23. Thai D K, Kim S E, Lee H K. Effects of reinforcement ratio and arrangement on the structural behavior of a nuclear building under aircraft impact. Nuclear Engineering and Design, 2014, 276: 228–240
24. Taerwe L, Matthys S. Fib Model Code for Concrete Structures. Berlin: Wiley, 2010
25. Chiorino M A, Lacidogna G. Revision of the design aids of CEB. Design manual on structural effects of time-dependent behaviour of concrete in accordance with CEB-FIP Model Code 1990. CEB Bulletin d'Information, 1993, 215: 297
26. Kim K. Application of SPH and ANN for prediction of the amount of concrete fragmentation under impact loadings. Dissertation for the Doctoral Degree. Busan: Korea Maritime and Ocean University, 2021
27. Cundall P A, Strack O D A. A discrete numerical model for granular assemblies. Geotechnique, 1979, 29(1): 47–65
28. Cundall P A. Formulation of a three-dimensional distinct element model—Part I. A scheme to detect and represent contacts in a system composed of many polyhedral blocks. International Journal of Rock Mechanics and Mining Sciences & Geomechanics Abstracts, 1988, 25(3): 107–116
29. Cundall P A, Hart R D. Numerical modeling of discontinua. Engineering Computations, 1992, 9(2): 101–113
30. Kim K, Lee M, Park J, Lee J. Evaluation of lateral resistance for caisson with RC piles encased by riprap. Structures, 2023, 50: 1089–1099
31. Lee S W. Influence of surface topography on interface strength and counterface soil structure. Dissertation for the Doctoral Degree. Atlanta: Georgia Institute of Technology, 1998
32. Kragelski I, Dobychin M, Kombalov V. The calculation framework of the friction and wear. Mashynostroenie, 1977, 256–260
33. Svanberg A, Larsson S, Mäki R, Jonsén P. Full-scale simulation and validation of wear for a mining rope shovel bucket. Minerals, 2021, 11(6): 623
34. KDS 64 10 10. Design Standards of Harbor and Fishery Ports. Seoul: Ministry of Oceans and Fisheries, 2023
35. Moghadam R E, Shafieefar M, Akbari H. A probabilistic approach to predict wave force on a caisson breakwater based on Bayesian regression and experimental data. Ocean Engineering, 2022, 249: 110945
36. Goda Y. Random Seas and Design of Maritime Structures. Singapore: World Scientific Publishing Company, 2010, 33: 732
37. Seo J, Yi J, Park W, Won D. Dispersion characteristics of wave forces on interlocking caisson breakwaters by cross cables. Journal of Korean Society of Coastal and Ocean Engineers, 2015, 27(5): 315–323
38. KDS 14 20 20. Korea Design Standard Ministry of Land. Infrastructure and Transport. Seoul: Ministry of Land, Infrastructure and Transport, 2021